



A highly efficient and stable oxygen reduction reaction on Pt/CeO_x/C electrocatalyst obtained *via* a sacrificial precursor based on a metal-organic framework



Yun Luo ^a, Laura Calvillo ^b, Carole Daiguebonne ^c, Maria K. Daletou ^d, Gaetano Granozzi ^b, Nicolas Alonso-Vante ^{a,*}

^a IC2MP, UMR-CNRS 7285, University of Poitiers, 4 rue Michel Brunet, 86022 Poitiers, France

^b Department of Chemical Sciences, University of Padova, Via Marzolo 1, 35131 Padova, Italy

^c INSA, UMR-CNRS 6226, 20 Avenue des Buttes de Coësmes, 35708 Rennes, France

^d Foundation of Research and Technology, Hellas-Institute of Chemical Engineering Science, Stadiou Str., Platani Rion, Patras GR-26504, Greece

ARTICLE INFO

Article history:

Received 12 November 2015

Received in revised form 21 January 2016

Accepted 10 February 2016

Available online 12 February 2016

Keywords:

MOF

Pt nanoparticles

Pt/Pt/CeO_x/C nanocomposite

ORR

Oxides

ABSTRACT

Advanced Pt/CeO_x/C nanocomposite, where C = porous carbon and multi-walled carbon nanotube (MWCNT), was synthesized using a precursor based on Ce-containing metal organic framework (MOF), *via* carbonyl chemical route, followed by heat-treatment at 900 °C under argon atmosphere. Based on the analyses of powder X-ray diffraction (*p*XRD) data, and *via* the Williamson-Hall method, the lattice parameter, stacking fault and micro-strain values on Pt/CeO_x/C was found to decrease, whereas the crystallite size increased with respect to the as-prepared sample. Combined with the results of transmission electron microscopy (TEM), these changes were related to the *in-situ* formation of intimately contacted Pt/CeO_x nanoparticles (NPs), well-dispersed onto MWCNT support. However, both the *p*XRD and TEM results showed that the Pt NPs were agglomerated upon heating and finally detached from the support in the MOF-free samples. Thus, MOF could protect Pt nanoparticles (NPs) from agglomeration at high temperature. The X-ray photoelectron spectroscopy (XPS) showed that the Pt surface was less oxidized in Pt/CeO_x/C nanocomposite in comparison to as-prepared and MOF-free samples. Moreover, only the Ce³⁺ was detected in the nanocomposite. These facts together with Raman spectroscopy and surface electrochemistry experiments assessed the stabilization of the electronic state of Pt⁰ and Ce³⁺ via the interaction between Pt and CeO_x. In addition, enhanced catalytic activity towards the oxygen reduction reaction (ORR) was observed in acid medium. The specific and mass activity at 0.9 V/RHE on Pt/CeO_x/C were *ca.* 1279 μA cm⁻²_{Pt} and 870 mA mg⁻¹_{Pt}, respectively, *ca.* 10–11 fold higher than commercial Pt/C (Johnson Matthey, JM) in half-cell. Accelerating durability tests (ADT), after 16,000 potential cycles, demonstrated higher stability of Pt/CeO_x/C in contrast to oxide-free and Pt/C (JM) catalyst. Compared with other homemade or commercial Pt/C (JM) cathodes, the innovative cathode catalyst showed enhanced cell performance in a H₂/O₂ micro-laminar flow fuel cell system.

© 2016 Elsevier B.V. All rights reserved.

1. Introduction

The sluggish kinetics of the oxygen reduction reaction (ORR) occurring at the cathode of fuel cells (FCs) represent a real challenge which is actually addressed by a fine tailoring of new ORR catalysts. Pt-based catalysts, mostly applied and studied for their high efficiency with respect to other Pt-free catalysts in acid medium [1], consist of Pt nanoparticles (NPs) supported onto different supports,

e.g., carbon, oxides and carbon/oxides composites [2]. However, a big issue is associated to the high cost and limited availability of Pt. In order to significantly reduce the amount of Pt loading, several strategies have been undertaken, e.g., alloying Pt with other metals. Recently, Pt₃Y alloy was theoretically predicted as the most efficient and stable catalyst for ORR [3]. This expectation was confirmed on a Pt₃Y bulk electrode tested in acid medium [3,4]. Pt₅Gd bulk alloy also showed excellent ORR activity and stability [5], implying that in general Pt alloys based on rare earth (RE) elements might be good candidates to improve the Pt catalytic performance in acid medium. Since then, many efforts have been devoted, by different research groups, to the synthesis of Pt NPs containing RE

* Corresponding author.

E-mail address: nicolas.alonso.vante@univ-poitiers.fr (N. Alonso-Vante).

elements [6–8]. However, up to now, no evidence of the formation of Pt-RE nanoalloys *via* chemical routes has been obtained, even at high temperature, e.g., 900 °C [6]. The only exception was the Pt_xY nanoalloy prepared *via* a physical method, using magnetron sputter agglomeration gas [9]. By employing the chemical route, instead, a large amount of RE oxides (RE=Y and Gd) was confirmed to be present on the Pt NPs surfaces [7]. However, it is very interesting to note that also RE oxides can induce a positive effect onto Pt NPs, thus enhancing the ORR process [6–8]. In previous works, we demonstrated that the ORR activity and stability of Pt-M₂O₃/C (M=Y and Gd; C=Vulcan XC-72) can be increased after heat-treatment (HT) [10]. Such a phenomenon has been associated to Pt surface defects induced by the RE oxides upon heating [11]. However, we have found that Pt-M₂O₃/C catalysts, prepared from MCl₃ precursors, *via* the carbonyl chemical route [12], are aggregated if HT is higher than 500 °C, leading to reduction of the Pt active surface and thus to a lower ORR activity. It is then necessary to tailor novel process to produce Pt-M₂O₃/C catalysts, protecting Pt NPs from agglomeration at temperatures higher than 500 °C.

Metal-organic frameworks (MOFs) [13], known also as coordination polymers, are crystalline micro- or macro-porous materials, constructed by metallic ions that act as lattice nodes and are held in place by multidentate organic ligands. They have been studied in gas-separation [14], storage [15], luminescence [16], magnetism [17] and catalysis [18]. Regarding their application in catalysis, there are two main trends, *i.e.* their direct utilization as a catalyst [19,20] or as a support/host for metal NPs [21]. In the former case, the ligands serve for tailoring the charge of the metal centers responsible as catalytic sites. In the latter case, noble metal NPs could be captured or supported by a MOF [21], which represent the actual catalytic sites either in catalysis [22] and photocatalysis [23]. An alternative route concentrates on using a MOF as a sacrificial precursor to synthesize powder catalysts after heat-treatment at temperature higher than 600 °C, under inert atmosphere [24–28]. The MOF can be carbonized as oxide/carbon composite or porous carbon. For example, Fe/N/CF composite can be prepared based on MOF [25]. The porous carbon from heat-treated from a nitrogen-containing isoreticular MOF was studied for its high porosity and capacitance [28]. Compared with applications in chemistry and photocatalysis, a few works, devoted to the utilization of MOF in electrocatalysis, have been published. For instance, Jahan et al. reported porphyrin-based MOF grafting on graphene for ORR in alkaline medium [29]. Yang et al. prepared a MOF-based electrocatalyst for ethanol oxidation reaction in acid medium [13]. MOF sacrificial precursor at 900–1000 °C have been used to template Fe graphene/carbon-nanotubes nanocomposites, resulting in an efficient catalysts towards ORR [27]. However, none of these systems was studied as a Pt-based electrocatalyst for FCs systems, nor the catalytic sites, efficiency and stability were investigated, to the best of our knowledge, in detail.

In this work, we focus on the synthesis of novel nanocarbon composites with Pt-RE oxide NPs *via* a MOF sacrificial precursor and on the study of their activity and stability towards ORR. The Ce(HATPT)(ATPT)-nH₂O (ATPT=2-aminoteraphthalate) MOF [30], hereafter denoted as MOF(Ce), was used as sacrificial precursor to prepare a nanocomposite Pt-CeO_x/C electrocatalyst. The choice of MOF(Ce) was based on the following reasons:

- As a member of the Ln(HATPT)(ATPT)-nH₂O (Ln=La – Eu except Pm) family, MOF(Ce) estimated specific surface area is around 2100 m² g⁻¹, which is one of the most porous MOF structures involving RE elements so far obtained [30]. According to the literature [24–28], one can anticipate that, after carbonization, the MOF(Ce) structure can be transformed at high temperature (e.g., 900 °C) into a porous carbon mixed with Ce oxide. This new

oxide/carbon composite support is expected to impact on the electrochemical performance of the final electrocatalysts.

- MOF(Ce) structure is solely composed of Ce³⁺ metal centers, which might eventually decompose into CeO_x. Recently, Masuda et al. reported that Ce³⁺ was responsible for Pt⁰ rich NPs surface, resulting in enhanced ORR activity in acid [31]. The authors explained the enhanced activity to the inhibition of surface Pt oxidation in presence of Ce³⁺ [31].
- As reported previously [30] the herein adopted MOF structure starts to decompose at temperature higher than 400 °C under nitrogen flux, resulting in a porous nanocarbon, which is expected to stabilize the Pt NPs against agglomeration.

Herein, we report the synthesis *via* carbonyl chemical route [12] of an innovative Pt/MOF(Ce)/MWCNT composite system, (where MWCNT = multiwall carbon nanotubes), which has been subsequently subjected to a heat-treatment at 900 °C to provide a final Pt/CeO_x/C (C = porous carbon with MWCNT) nanocomposite electrocatalyst. The as-prepared and heat-treated samples, at 400 °C and at 900 °C, are further designated as SMOF-1, SMOF-2 and SMOF-3, respectively. The impact of the MOF(Ce) was studied in detail, and compared to MOF-free samples, *i.e.* as prepared Pt/MWCNT composite (SCNT-1), heat-treated Pt/MWCNT at 400 °C (SCNT-2) and at 900 °C (SCNT-3). A quite unique nanocomposite structure was found in SMOF-3, and its activity towards ORR was systematically studied. Finally, it was tested as a cathode catalyst in a micro-laminar flow fuel cell (μ LFFC) in acid medium.

2. Experimental

2.1. Preparation of SMOFs and SCNTs samples

The preparation of oxidized MWCNT was already described in the literature [32]. The micro-crystalline powder of MOF(Ce) was prepared *via* a published method [30]. The synthesis of SMOFs samples was realized *via* carbonyl chemical route. 72.1 mg Na₂PtCl₆·6H₂O (99.9%, Alfa Aesar) and 63.1 mg sodium acetate (99.9%, Alfa Aesar) were mixed in a flask with 25 mL methanol (99.9%, Alfa Aesar), sealed under CO (99.99%, Air Liquide) at 55 °C for 24 h. Then the flask was cooled down to room temperature, followed by adding 115.2 mg MWCNT and 14.2 mg MOF(Ce) into the flask under N₂ (99.99%, Air Liquide). The system was sealed under this condition with continuous stirring for 12 h. The solvent was evaporated at 80 °C under N₂. The obtained powder was dried at 60 °C overnight under air. The obtained catalyst, rinsed by ultra-pure water (18.2 MΩ cm², Millipore), was SMOF-1 sample. The SMOF-1 powder was heated at 50 °C under Ar (99.99%, Air Liquide) for 60 min, followed by heat-treatment increasing the temperature at a heating rate of 10 °C min⁻¹ from 50 to 400 °C or 900 °C and maintained at this temperature for 2 h under Ar, noted as SMOF-2 and SMOF-3 samples, respectively. Finally, the powder was cooled down to room temperature under Ar. Thereafter, the powder was rinsed by ultra-pure water (18.2 MΩ cm, Millipore).

The synthesis of SCNTs samples was the same as that of SMOF system, except that no MOF(Ce) was added into the system during the synthesis. The protocol for heat-treatment was the same to that of SMOF. The as-prepared and heat-treated samples at 400 °C and 900 °C are noted as SCNT-1, SCNT-2 and SCNT-3, respectively.

The synthesis of SMOF-4 sample was the same as that of SMOF-1 sample, except that 125 mg of pre-treated support was added into the system during the synthesis. This support was prepared by heating the mixed MOF(Ce) and MWCNT at 900 °C under Ar for 2 h.

The synthesis of SMOF-5 and SMOF-6 samples followed the same procedure to that of SMOF-3, except that 125 mg of Vul-

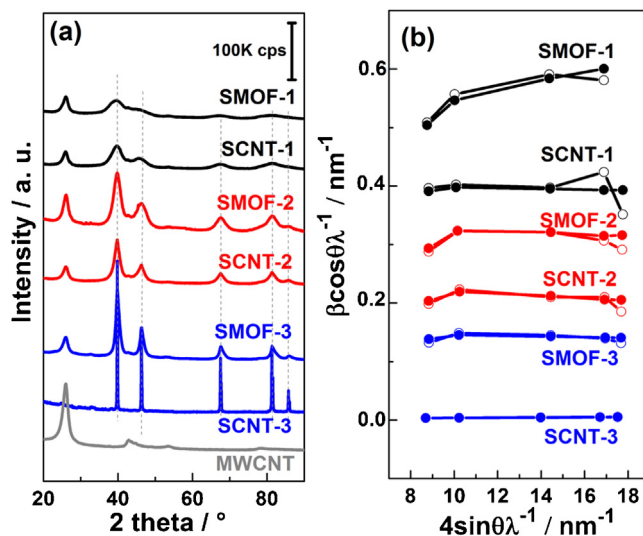


Fig. 1. (a) pXRD patterns, (b) Williamson-Hall plots for SMOFs and SCNTs systems. Empty symbols represent the 5 Bragg peaks data, and the filled ones the fitted data.

can XC-72 and MWCNT-m were used as substrate materials. The preparation of MWCNT-m was as reported in literature [33].

2.2. Physical and chemical characterizations

Powder X-ray diffraction patterns (pXRD) measurements of catalysts powders were performed on an EMPYREAN PANALYTICAL X-ray diffractometer using Cu K α radiation ($\lambda = 0.15406$ nm). The XRD spectra were obtained using high resolution with the step-scanning mode, a narrow receiving slit (1/16°), and a counting time of 240 s per 0.05° from 12° to 120°. By referring to the Joint Committee on Powder Diffraction Standards International Center for Diffraction data (JCPDS-ICDD) database, the structural phase was identified. Prior to analysis, the 2θ and instrumental broadening for all the pXRD patterns were corrected by the pattern of LaB₆ measured at the same experimental condition. The lattice parameter, a_{fcc} , of catalysts was estimated from Eqs. (1) and (2).

$$d_{hkl} = \frac{\lambda}{2\sin\theta} \quad (1)$$

$$d_{hkl} = \frac{a_{fcc}}{\sqrt{h^2 + k^2 + l^2}} \quad (2)$$

where $\lambda = 0.154056$ nm, θ diffraction angle in radians, hkl Miller indices, and d_{hkl} the interplanar distance. In this work, a , was the average value of calculations of 5 typical diffraction peaks belonging to Pt face centered cubic. Strain effect (ε), stacking fault (α) and crystallite size (L_v) were estimated based on the Williamson-Hall

Table 1

Parameters evaluated from pXRD patterns: lattice parameter (a_{fcc} /nm), crystallite size (L_v /nm), stacking fault (α %), and micro-strain value (ε %).

Sample	a_{fcc}	L_v	α	ε
SMOF-1	0.3942	2.63	1.95	1.17
SMOF-2	0.3922	3.98	1.85	0.25
SMOF-3	0.3915	7.65	0.45	0.03
SCNT-1	0.3928	2.71	1.43	0.02
SCNT-2	0.3915	5.25	1.05	0.02
SCNT-3	0.3972	625	0.001	0.02
Pt/C (JM) ^a	0.3927	4.6	—	0.023

^a Data extracted from literature [44].

method, following the same calculation procedure in our previous works via Eq. (3) [7,34].

$$\frac{\beta\cos\theta}{\lambda} = \frac{k}{L_v} + \frac{K_{hkl}}{a_{fcc}}\alpha + \frac{4\sin\theta}{\lambda}\varepsilon \quad (3)$$

where β is the full-width at half-maximum (FWHM) of the diffraction peak, $\lambda = 0.154056$ nm, θ diffraction angle in radians, k is the Scherrer constant considering equal to 1, $K(111) = 0.43$, $K(200) = 1$, $K(220) = 0.71$, $K(311) = 0.45$ and $K(222) = 0.43$. Each diffraction peak was fitted with Pearson VII function. This function aids to obtain the parameters such as a , θ_{hkl} and full-width at half-maximum experimental (FWHM, β_{exp}) applied at the Pawley method [35], Eqs. (4)–(8).

$$I_C = \frac{I_{hkl}}{(1 + \kappa \times \Delta\theta^2)^m} \quad (4)$$

$$\kappa = \frac{4(2^{1/m} - 1)}{\beta_{exp}^2} \quad (5)$$

$$I_C = I_{hkl} \left\{ (1 - m) \times \exp(-\ln 2 \times 4\kappa_I^2) + \frac{m}{1 + 4\kappa_I^2} \right\} \quad (6)$$

$$\kappa_I = \frac{\Delta 2\theta}{\beta_{exp}} \quad (7)$$

$$\Delta 2\theta = 2\theta_i - 2\theta_{hkl} \quad (8)$$

where I_C is the calculated profile intensity of a data point i in Eq. (8), I_{hkl} is the peak height. The κ , κ_I , θ_{hkl} , a , β_{exp} , and m constants were extracted by Leverberg-Marquardt algorithm implemented in Eq. (3) using Fitik (free software) [36]. The mean particle size was investigated by transmission electron microscopy (TEM) on a JEOL microscopy (JEM-2001). The samples were dispersed in ethanol, then a drop of such a solution was placed on a copper grid covered by carbon film and the ethanol was evaporated. For all the catalysts, the particle diameter in TEM images was evaluated by ImageJ free software. The particle size distribution histograms were obtained by 500 single and spherical nanoparticles (with diameter lower than 50 nm) counting on different TEM images. The composition and mass metal loading of the samples were evaluated using ICP-OES (Optima 2000 DV, Perkin-Elmer) technique. The metal mass was ca. 16 wt% of Pt and 2 wt% of Ce in SMOF-1 and SMOF-2, ca. 19 wt% of Pt and 2 wt% of Ce in SMOF-3, ca. 20 wt% of Pt in SCNT-1 and SCNT-2 sample, ca. 46 wt% of Pt in SCNT-3 sample. Photoemission data was acquired in a custom designed ultrahigh vacuum (UHV) system equipped with a VG MK II Escalab electron analyzer, working at a base pressure of 10^{-10} mbar. Core level photoemission spectra (Pt 4f and Ce 4d, pass energy 20 eV) were taken at room temperature in normal emission using a non-monochromatized Mg K α anode. Powder samples were suspended in ethanol and drop casted on conductive carbon tape. After drying in air, the samples were introduced in the ultrahigh vacuum system, outgassed for 1 h, and finally analyzed. There was no evidence for charging. The spectrometer energy calibration was carried out by using a gold sample (Au 4f at 84 eV). The Pt 4f photoemission lines were separated into three different chemical-shifted components (Pt⁰, Pt²⁺ and Pt⁴⁺), after Shirley background removal, to identify the predominant oxidation state of Pt. For the deconvolution of the peaks, Voigt shaped peaks were used, imposing a FWHM in the 1–1.5 eV range, except for the metallic Pt component where an asymmetrical shape was used. The C 1s peak was separated into five single chemical shifted components. An asymmetrical shape was used for the sp² component, whereas symmetrical Voigt functions were used for the sp³ component and the oxygenated groups. Raman spectra were recorded on a Horiba Jobin Yvon Labram HR800UV Raman spectrometer, equipped with an Ar⁺ laser (Melles Griot) as light source and with a CCD cooled detector. The laser source frequency was

514.5 nm line. And the obtained spectra were analyzed by Fityk free software.

2.3. Electrode preparation and electrochemical measurement in half-cell

The electrochemical measurements in half-cell were performed in 0.1 M HClO₄ at 25 °C. The glassy carbon electrode (GCE) as rotating disk electrode (RDE) with 3 mm diameter (geometric surface of 0.071 cm²), was used as the working electrode (WE), preliminary polished using alumina powder. The reference electrode was a reversible hydrogen electrode (RHE). And a piece of glassy carbon was used as counter electrode. 10 mg of catalytic powder was added into 0.25 mL Nafion® solution (5 wt%, Aldrich) and 1.25 mL isopropanol/ultra-pure water (1/3, v/v) to obtain an ink. 3 μL of the catalytic ink was then deposited onto the GCE used as WE. The deposit was further dried under air on RDE at a speed of 700 rpm. The reproducibility of the deposition method used in this study was checked for 10 deposits on RDE. The obtained active surface values based on hydrogen underpotential deposition surface area was 2.99 ± 0.99 cm² for 10 ink deposits on WE, calculated from cyclic voltammograms (described later). Electrochemical measurements were recorded using an Autolab Potentiostat/Galvanostat and performed in a three-electrode standard electrochemical cell. 0.1 M HClO₄ aqueous solution was diluted from 70% HClO₄ (Suprapur, Merck) with ultra-pure water. The WE surface was firstly electro-cleaned by performing 20 voltammetric cycles at 50 mV s⁻¹ between 0.05 to 1.2 V vs. RHE to obtain stable cyclic voltammograms (CVs). CO-stripping voltammograms were performed using the following methodology. First, CO was adsorbed under a controlled potential (0.1 V vs. RHE) in a CO-saturated electrolyte for 10 min. Then the electrolyte was purged by bubbling N₂ for 30 min. Finally, CVs at a scan rate of 5 mV s⁻¹ were performed in the CO free electrolyte in the potential interval ranging from 0.05 to 1.2 V vs. RHE. The ORR activity was evaluated by recording linear sweep voltammograms (LSVs) at a scan rate of 5 mV s⁻¹ in the 1.0–0.2 V vs. RHE potential range in O₂-saturated (99.99%, Air Liquide) electrolyte using the RDE technique. The rotating rates of RDE for LSVs were 400, 900, 1600 and 2500 rpm. The kinetic current density was calculated with the Koutecky-Levich (K-L) Eq. (9) [37]:

$$\frac{1}{j} = \frac{1}{j_k} = \frac{1}{j_d} = \frac{1}{j_k} + \frac{1}{BC^0\omega^{1/2}} \quad (9)$$

where j is the current density, j_k the kinetic current density, j_d the diffusion current density, C° the concentration of molecular oxygen, ω the angular rate of rotating disk electrode. Linear fitting Eq. (9), j^{-1} vs. $\omega^{-1/2}$, j_d can be obtained from the slope and $\omega^{1/2}$. j_k could be derived, using Eq. (9). The active surface area (cm²) was calculated by the coulometry of the hydrogen under potential deposition (H_{upd}) or by the CO oxidation peak surface, using a charge of 210 and 420 μC cm⁻², respectively. The electrochemical surface area (ECSA), geometric surface area, ORR specific activity (SA), and mass activity (MA) are defined in Eqs. (10)–(13).

$$\text{ECSA} = \frac{\text{Active surface area (m}^2\text{)}}{\text{Pt mass (g)}} \quad (10)$$

$$\text{Geometric area} = \frac{6000}{\rho d} \quad (\rho = \text{Pt density}, d = \text{mean particle size}) \quad (11)$$

$$\text{SA} = \frac{\text{kinetic current (μA)}}{\text{Active surface (cm}^2\text{)}} \quad (12)$$

$$\text{MA} = \frac{\text{kinetic current (mA)}}{\text{Pt mass (mg)}} \quad (13)$$

For accelerated durability tests (ADT), the WE was submitted to CVs cycles at a scan rate of 50 mV s⁻¹ between 0.6 to 1.0 V vs. RHE in N₂-saturated electrolyte. Then 20 cycles of CV recorded at a scan rate of 50 mV s⁻¹ between 0.05 to 1.2 V vs. RHE in N₂-saturated electrolyte to evaluate the active surface area of aged catalyst. Finally, LSVs were recorded at scan rate of 5 mV s⁻¹ between 1.0 to 0.2 V vs. RHE in O₂-saturated electrolyte on RDE, to study the ORR kinetic.

3. Results and discussion

3.1. Characterizations of SMOF and SCNT samples

The power X-ray Diffraction (pXRD) patterns for all the catalysts are shown in Fig. 1a. In the as-prepared and heat-treated SMOF and SCNT samples, only the face centered cubic Pt phase, namely (111), (200), (220), (311) and (222) can be identified. The peaks belonging to carbon phase can be found with comparison of pXRD pattern of MWCNT [38]. It is worth to note that no diffraction peaks associated to the pristine MOF(Ce) structure are observed in MOF samples. In fact, according to the literature [30,39], MOF(Ce) loses its crystallinity but the highly porous framework remains intact during the dehydration process starting at 50 °C. Essentially, the temperature in the synthesis of SMOF-1 is higher than 50 °C. This explains why no diffraction peak from MOF(Ce) can be observed in the pXRD patterns. Based on the analyses of pXRD patterns via Williamson-Hall method, Fig. 1b, one can observe that $\beta \cos \theta \lambda^{-1}$ (where β is the integral peak width, θ the angle, and λ the diffraction wavelength) values are non-linear with $4 \sin \theta \lambda^{-1}$. This indicates that the diffraction peak broadening is affected by the crystallite size (L_v), micro-strains (ε) and stacking faults (α). The calculated lattice parameter (a_{fcc}), L_v , ε and α , for all catalysts, are summarized in Table 1. For SMOF systems, the a_{fcc} decreases, whereas L_v increases upon heat-treatment. This infers that lattice strain effect is enhanced from SMOF-1 to SMOF-3 samples, together with increased crystallite size. The fact that α is reduced upon heat-treatment, suggests less intrinsic or extrinsic stacking at the planes of Pt nano-crystals after heat-treatment, possibly related to morphology change. On the other hand, ε value is decreased from ca. 1.17% in the SMOF-1 to ca. 0.03% in SMOF-3, which should be linked to increased L_v , strongly supporting a surface healing process during heat-treatment [40]. Indeed, on oxide supported Pt NPs, e.g., Pt/Cr-TiO₂ [41], a lattice strain effect was reported, which has been associated to the enhanced ORR activity. However, for SCNT systems, as listed in Table 1, the a_{fcc} value decreases from SCNT-1 to SCNT-2 sample and increases in SCNT-3 sample, indicating that the lattice strain effect induced by heat-treatment in SCNT-2 disappears in SCNT-3. Besides, the L_v value increases moderately from ca. 2.71 nm in SCNT-1 to ca. 5.25 nm in SCNT-2, but increases drastically in SCNT-3. Further, α values slightly decrease from SCNT-1 to SCNT-2, but sharply decrease in SCNT-3. All these results suggest a great change in the Pt particle morphology during heat-treatment for SCNT samples. The ε value is constant for SCNT samples during HT suggesting that the Pt surface remains intact.

From TEM images, one observes that in SMOF-1 (Fig. 2a) Pt NPs are slightly agglomerated and are dispersed onto both MOF(Ce) framework and MWCNTs. Nanorods-like particles can also be found in this sample. The mean particle size (d) is ca. 2.0 ± 0.4 nm. After heat-treatment at 400 °C (Fig. 2b), spherical NPs are still supported on both MOF(Ce), and MWCNT with d = 3.1 ± 0.9 nm. However, some Ce oxides fragments can be observed in this sample (see arrows in Fig. 2b). Compared to SMOF-1, fewer nanorods-like particles can be observed in SMOF-2. For SMOF-3, several Pt agglomerations can be observed (not shown here) but most

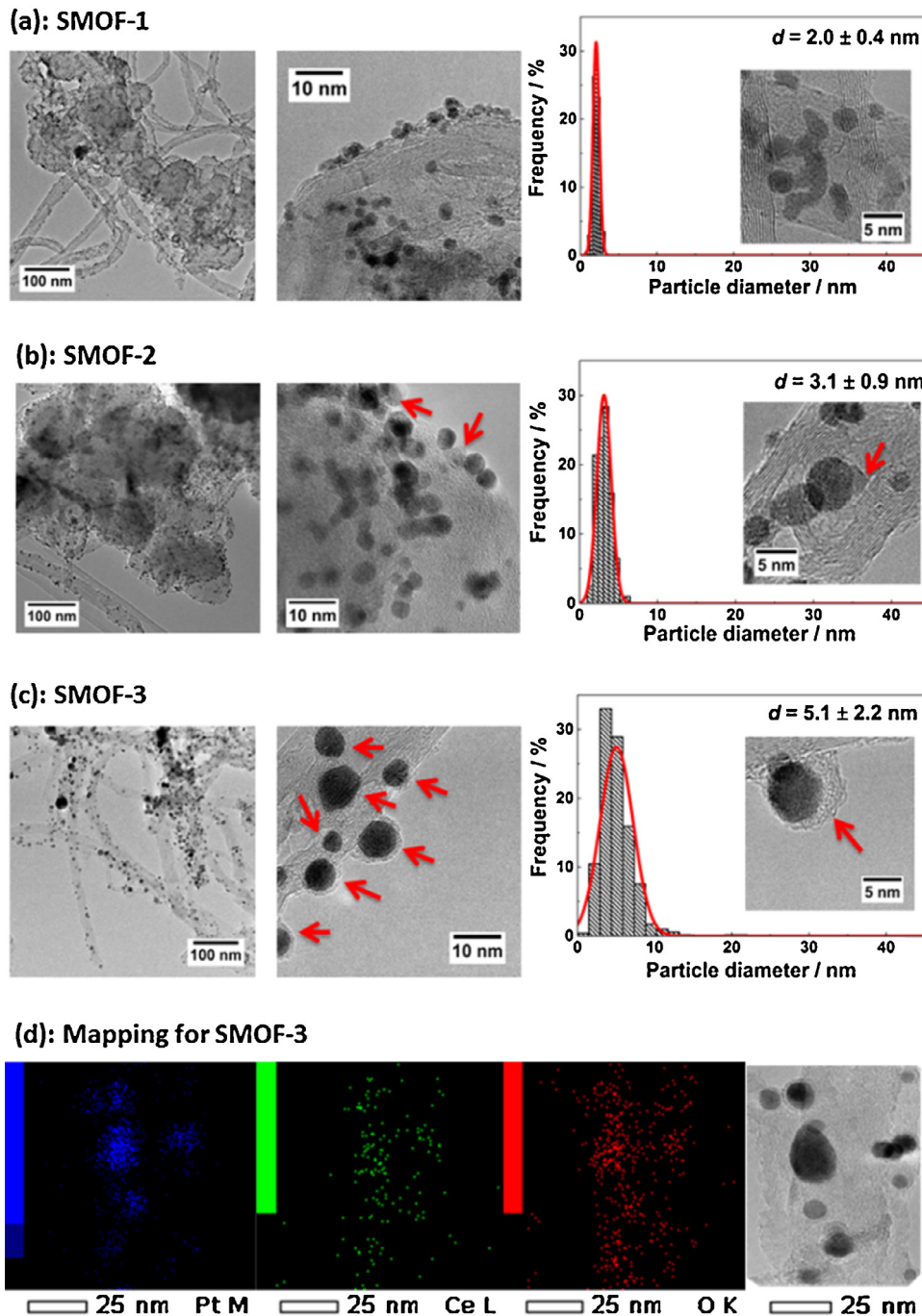


Fig. 2. TEM images and particle size distribution for (a) SMOF-1, (b) SMOF-2, (c) SMOF-3. (d) EDS mapping for SMOF-3. Insets: higher magnification of TEM image for SMOF samples.

spherical Pt NPs are homogeneously dispersed onto MWCNT with $d = 5.1 \pm 2.2 \text{ nm}$ (Fig. 2c). No MOF(Ce) framework can be detected by TEM in this sample. Taking the thermal stability of MOF(Ce) structure into account, amorphous carbon mixed oxide should be formed from its decomposition at 900°C [28,30]. The Pt NPs in SMOF-3 are coated by a layer (*ca.* 0.5–1.0 nm, highlighted by arrows in Fig. 2c), whose actual structure is hard to be revealed in absence of high resolution TEM images. Such a layer was found neither in SMOF-1 nor in SMOF-2 samples. However, using energy dispersive spectroscopy (EDS) mapping, see Fig. 2d, we can stress that Pt, Ce and O are intimately connected and form a nanocomposite system. The morphological evolution is in good agreement with the Williamson-Hall analyses of *p*XRD patterns for SMOF

samples during heat-treatment. The highest α value, in SMOF-1, should be associated to nanorods-like objects, since previous work revealed enhanced α value on nanorods-like for palladium with respect to spherical Pd NPs [34]. After heat-treatment, the number of nanorods is reduced, possibly inducing a decrease of α values. Moreover, the trend of L_v from *p*XRD corresponds to that of d from TEM (*cf.* Table 1). Concerning SCNT samples, it is very interesting to observe that the d of Pt NPs (*cf.* Fig. 3a–c) increases from SCNT-1 (*ca.* $2.3 \pm 0.4 \text{ nm}$) to SCNT-2 (*ca.* $4.8 \pm 1.7 \text{ nm}$), and becomes huge due to Pt agglomerations detached from MWCNT after HT-900 treatment (*ca.* $12 \pm 9 \text{ nm}$) in SCNT-3. TEM images also reveal that NPs in SCNT-2 are less aggregated than in SCNT-1, probably inducing a decrease of α .

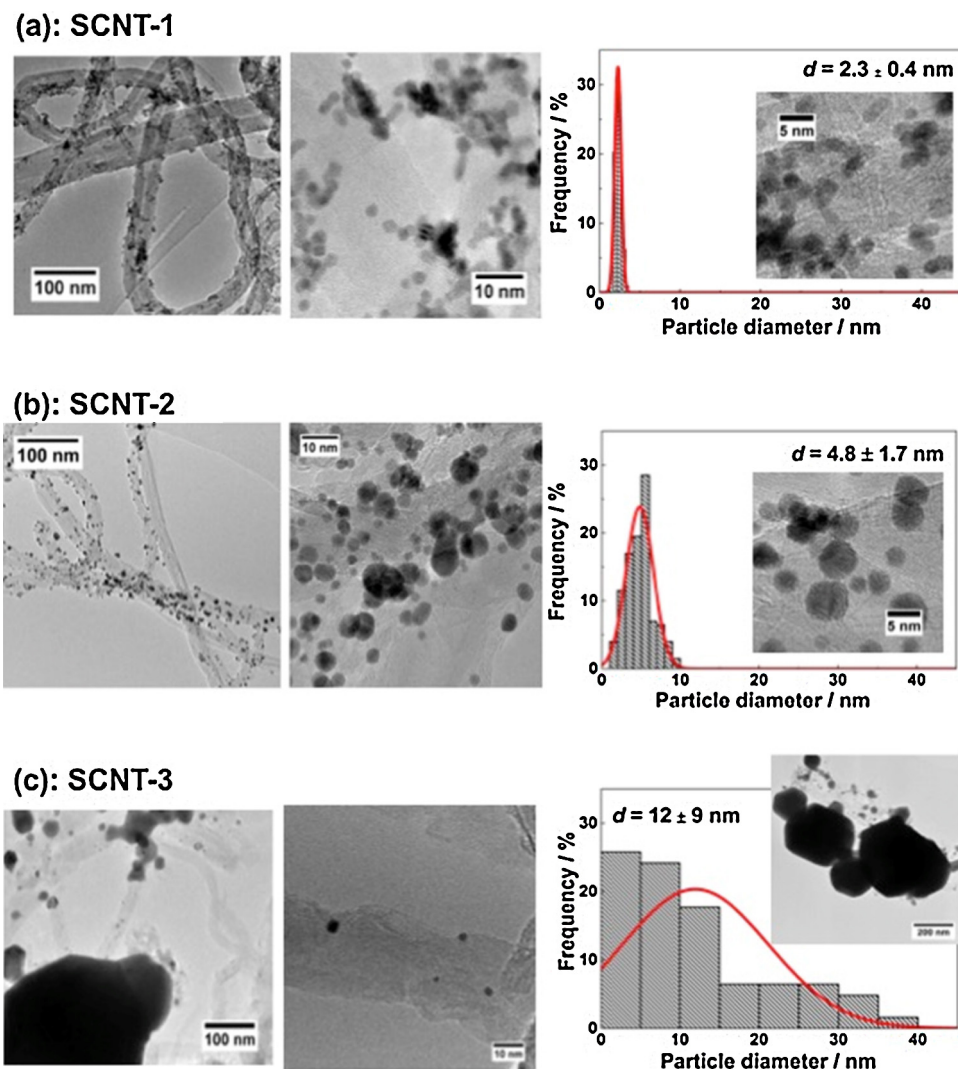


Fig. 3. TEM images and particle size distribution for (a) SCNT-1, (b) SCNT-2, (c) SCNT-3. Insets: higher magnification of TEM image for SCNT samples.

In both SMOF and SCNT cases, the d value progression is in agreement with L_v , it is worth to note that the L_v are higher than d for all the catalysts. One observes in Figs. 2 and 3, the presence of some non-spherical NPs (ex. nanorods, irregular agglomerates). These particles could not be taken into account in the determination of d . However, non-spherical (anisotropic) and agglomerated particles contribute to the diffraction peak broadening (β) of XRD diffraction peaks. The L_v was estimated from the Williamson-Hall method based on β , considering that the particles are isotropic, since it is hard to deconvolute the anisotropic or/and agglomeration impact from isotropic on β . Therefore, it is possible that the L_v is higher than d [42,43]. For example, Said-Galiyev et al. reported the L_v calculated from XRD is higher than d based on TEM, for both homemade and commercial Pt/C catalysts [44]. Weibel et al. revealed the same phenomenon for TiO₂ particles [45]. In the work of Langford et al., it was found that higher L_v than d occurs when the particle size distribution is wide [42]. Thus, the particle size evolution in SMOF with respect to SCNT systems, one can conclude a positive effect of MOF(Ce) in protecting Pt NPs from agglomeration at high temperature (e.g., 900 °C).

In order to obtain surface chemical composition of the catalysts, X-ray Photoemission Spectroscopy (XPS) data of the Pt 4f, C 1s, O 1s and Ce 3d photoemission lines for the SMOF and SCNT materials were taken. In Fig. 4 we summarize the most relevant data of the

SMOF materials. The Pt 4f, C 1s and Ce 3d peaks were separated into single chemical components in order to study any possible effect of both the support and the MOF(Ce) on the electronic properties of Pt NPs, as well as the effect of the thermal treatment at 900 °C under Ar atmosphere.

The Pt 4f peak (Fig. 4a) was separated into three different chemical-shifted components (Pt⁰, Pt²⁺ and Pt⁴⁺): as seen in Table S1-1 in Supporting information (SI), Pt⁰ is the predominant oxidation state in all the Pt catalysts (around 79–84%). However, all samples present a variable amount of oxidized species (Pt²⁺ and Pt⁴⁺), deduced from the Pt 4f_{7/2} peaks at a binding energy (BE) in the range 72.6–74.7 eV. The fact that there is a considerable amount of oxidized species is in general in tune with the relative small sizes of the Pt NPs. The treatment at 900 °C for SMOF-3 sample under Ar atmosphere results in a decrease of oxidized species, which can be related to the larger size of the Pt NPs (see TEM data) and also to a specific interaction with the Ce component obtained by the MOF(Ce) decomposition (see below) [31]. In the case of SCNT samples (not reported), the only significant change is associated to a small shift of the Pt 4f_{7/2} peak of SCNT-3 toward lower BE with respect to SMOF-3 due to the relevant increase of the Pt NPs size, as already evidenced by the TEM analysis [46,47].

The C 1s peak (Fig. 4b) of the investigated SMOF samples was separated into five single chemical shifted components. The most

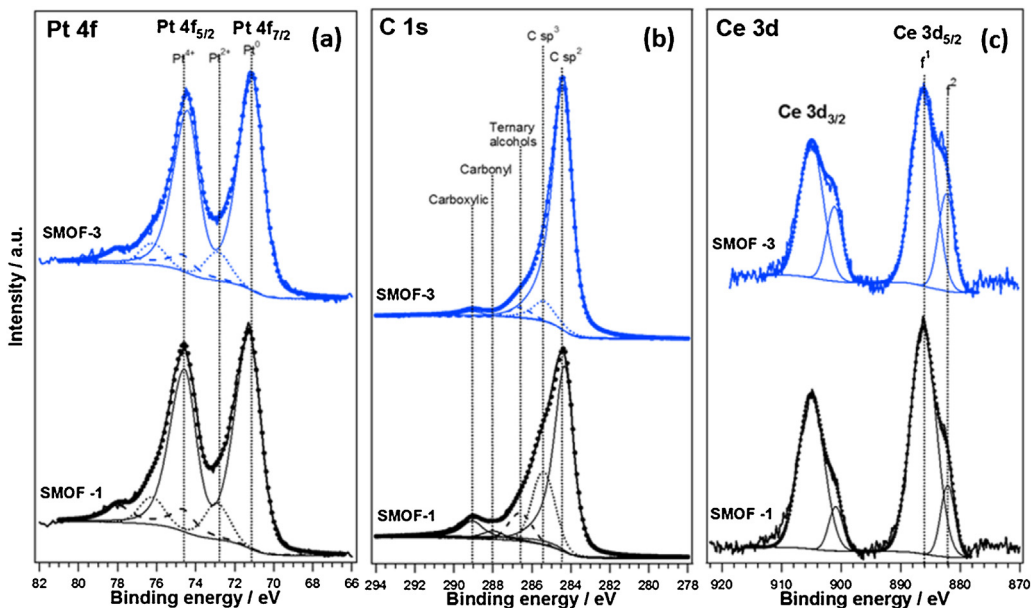


Fig. 4. (a) Pt 4f, (b) C 1s and (c) Ce 3d XPS spectra, as well as the separation of the Pt 4f, C 1s and Ce 3d regions into single chemical components, for the SMOF samples.

intense peak, centered at 284.4 eV, is associated to graphitic carbon ($C\ sp^2$), while the peak centered at 285.3 eV is associated to sp^3 hybridized carbon atoms ($C\ sp^3$). The samples also show peaks at 286.5, 288 and 289.1 eV, attributed to ternary alcohols, carbonyl and carboxylic groups, respectively (see Table S1-2). The treatments at 900 °C resulted in the reduction of the surface oxygenated species.

Ce 3d XPS line is usually rather complex because it is characterized by the contribution of several initial and final states for each oxidation state of Cerium (Ce^{3+} and Ce^{4+}) [48]. The XPS pattern observed in Fig. 4c is only compatible with the complete absence of Ce^{4+} : the Ce 3d_{5/2} peak can be fitted with two components, at 882.1 and 886.2 eV, both associated to Ce^{3+} (Table S1-3). These two components are assigned to two different final states where the 4f¹ and 4f² configurations are strongly mixed. No component

associated to Ce^{4+} was used in the fit because the absence of a separate peak at around 916 eV is indicative of the absence of Ce^{4+} species. The analysis of SMOF-3 sample subjected to the treatment at 900 °C indicates that the structure of the Ce electronic state is slightly modified with respect to SMOF-1, in any case being absent of any fingerprint from Ce^{4+} : the two components associated to the different final states have different relative intensities (see the fitting in Fig. 4c and Table S1-3), indicating small differences in the coordination of the Ce^{3+} ions, even if the difference cannot be easily rationalized. We can propose (see below) to associate such a change to the passage from Ce^{3+} ions attached to the MOF to Ce^{3+} associated to reduced ceria (CeO_x) in contact with the Pt NPs. In fact, the tendency of CeO_x to interact with Pt surfaces has been demonstrated by rigorous surface science studies on $CeO_x/Pt(111)$

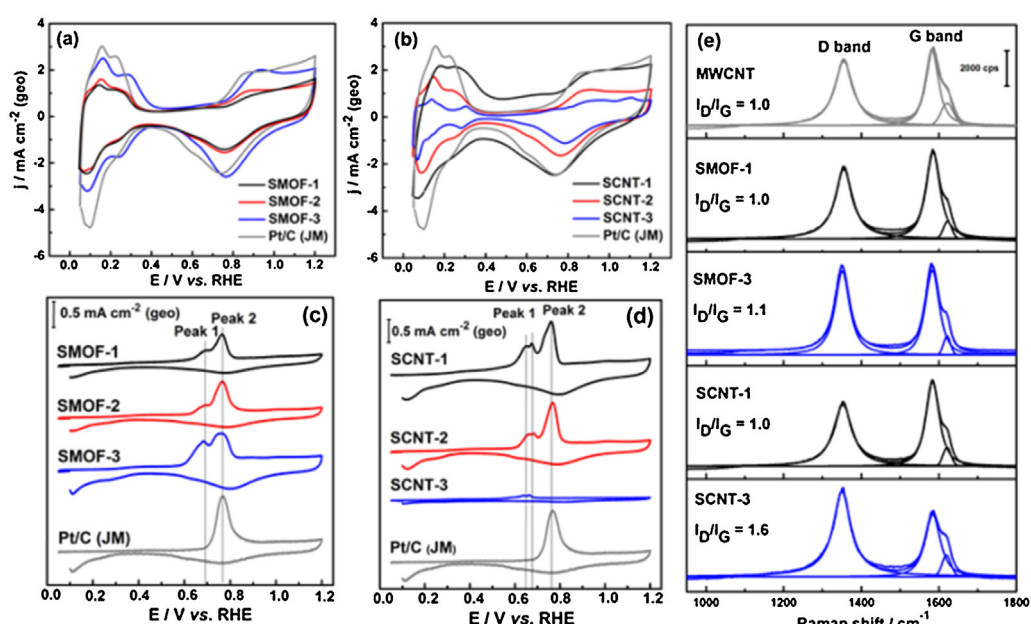


Fig. 5. CVs (a and b) recorded at scan rate of 50 mV s⁻¹; and CO-stripping voltammograms (c and d) at scan rate of 5 mV s⁻¹ in HClO₄, for SMOFs (a and c), and SCNTs (b and d) samples. (e) Raman spectra for MWNCT, SMOF and SCNT samples.

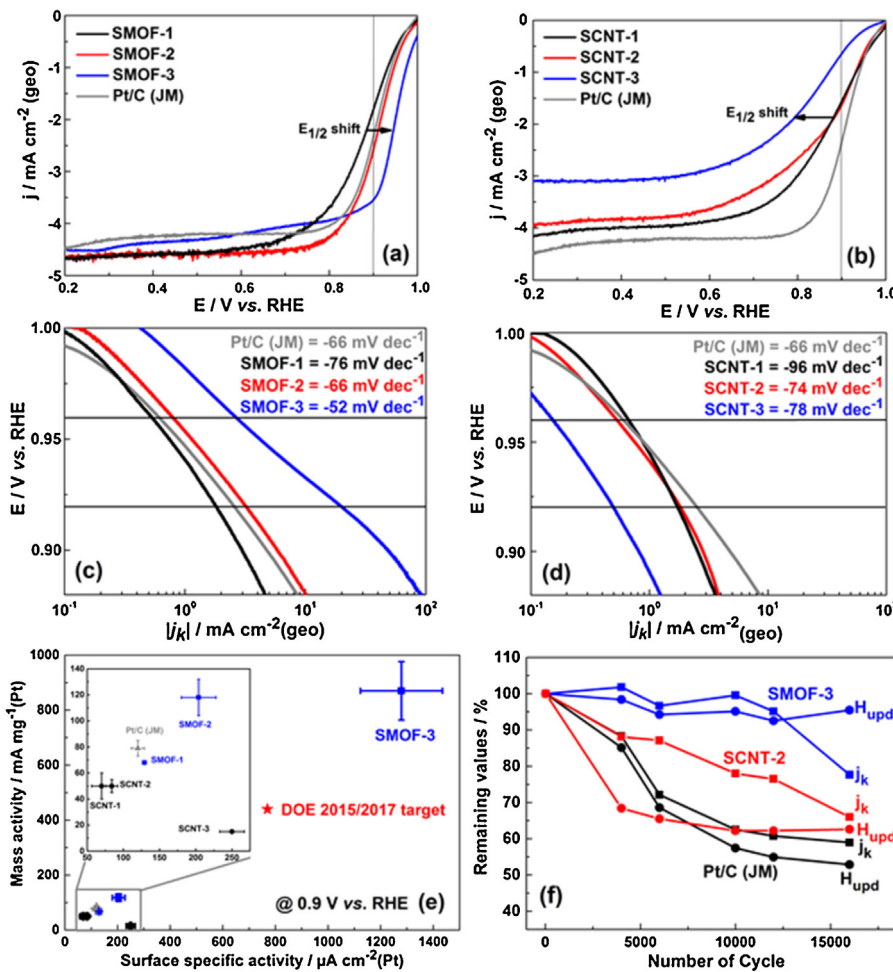


Fig. 6. LSVs recorded at scan rate of 5 mV s⁻¹ in O₂-saturated HClO₄ for (a) SMOFs and (b) SCNTs, at 25 °C at a rotation rate of 900 rpm. Mass-transfer corrected Tafel plots, derived from ORR polarization curves for (c) SMOFs and (d) SCNTs samples. (e) Mass and surface specific activity for SMOFs, SCNTs, Pt/C (JM) catalysts compared to the DOE 2015/2017 target; (f) Remaining H_{upd} and j_k (@ 0.9 V vs. RHE) values obtained during ADT for SMOF-3, SCNT-2 and Pt/C (JM) catalysts.

model systems, where the existence of ultrathin CeO_x layers on the Pt surface has been observed [49].

One can thus conclude from XPS that a nanocomposite formed by CeO_x, porous carbon and Pt NPs is present after the heat treatment at 900 °C in samples prepared by carbonyl chemical route adopting sacrificial MOF(Ce). A mechanism of the formation of such nanocomposite in SMOF-3 could be attempted as follows: in SMOF-1, the MOF(Ce) framework plays a role as substrate to support the Pt NPs. In this case the full coordination of the Ce³⁺ ions within the MOF framework is avoiding the oxidation to Ce⁴⁺ and the direct interaction with Pt. After heat treatment at 900 °C in Ar, the MOF framework is totally destroyed, forming a Pt/CeO_x/C(porous carbon + MWCNT) nanocomposite where porous carbon is somehow embedding the metallic components. We can suggest that at this stage the PtO_x layer around the Pt NPs is transformed into Pt/CeO_x. Interestingly enough, the porous carbon matrix fully protects the Ce³⁺ from full oxidation. This is a quite unique behavior because the tendency of Ce³⁺ to form Ce⁴⁺ is rather high and even small traces of oxygen in standard Ar would be sufficient to partially oxidize Ce³⁺ in absence of such a protection.

3.2. Surface electrochemistry for SMOF and SCNT samples

The surface electrochemistry of SMOF and SCNT samples was firstly studied by cyclic voltammetry (CV) and the results are reported in Fig. 5. The electrochemical surface area (ECSA) was

calculated from the hydrogen under-potential deposition (H_{upd}) region. Fig. 5a shows that the ECSA(H_{upd}) increases with the heat treatment, that is, from SMOF-1 (ca. 48 m² g⁻¹) to SMOF-3 (ca. 72 m² g⁻¹) (Table S2). It should be noted that the ECSA(H_{upd}) increases with the heat treatment, whereas the geometric area calculated from the average particle size decreases (see Fig. 2 and Table S2). This contradictory effect could be explained by the better dispersion of the Pt NPs obtained after the decomposition of the MOF(Ce) during the heat treatment at 900 °C, as seen by TEM. The presence of the CeO_x in SMOF-3 should promote the hydrogen adsorption-desorption of Pt NPs surfaces. It was reported that more H atoms can be adsorbed per Pt atom in cerium oxide supported Pt catalyst [11]. On the other hand, the electroactive surface area determined for CNT samples from the H_{upd} region (Fig. 5b) decreases with the heat treatment due to the agglomeration of the Pt NPs with the heat treatment (Table S2). The low ECSA (H_{upd}) calculated for the SCNT-3 sample is attributed to the loss of the carbon support (cf. Pt mass of SCNT-3 in experimental section) during the heat treatment, leading to the total agglomeration of Pt NPs (cf. TEM images in Fig. 3c). Besides, compared with the barely changed capacitance in SMOF samples, the double-layer behavior of SCNTs is not constant, probably suggesting deterioration of carbon support. These results reveal that the presence of MOF(Ce) could stabilize and avoid the agglomeration of Pt NPs during heat-treatments.

To further understand the role of MOF(Ce) precursor, CO-stripping voltammograms were performed. All the synthesized

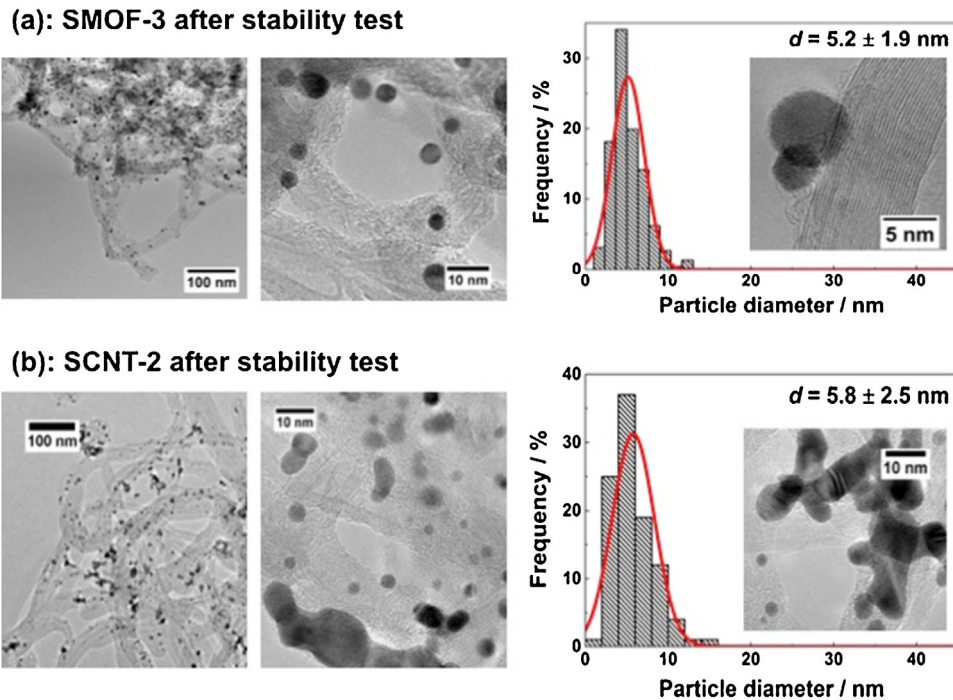


Fig. 7. TEM images and particles size distribution curves for (a) SMOF-3 and (b) SCNT-2 samples after ADT. Zoom of particles (insets).

SMOF samples (Fig. 5c) showed two CO oxidation peaks at around 0.68 V and 0.76 V, respectively. The multi-peaks in CO-stripping have been associated in the literature to various aspects, such as Pt NPs size, [50,51] facets [52,53] and/or agglomeration [54] effects. Among them, the size effect should be negligible, since the peak shape and potential is barely changed with the increase of particle size, cf. SMOF-1 and SMOF-2 in Fig. 5c. Taking into account the morphology and distribution of the Pt NPs deduced from TEM, the

two peaks could be related to the CO oxidation on Pt NPs interacting with different substrate domains. According to the literature, peak 1 could be attributed to the CO-oxidation on Pt NPs interacting with the graphitic domain (sp^2) of MWCNT and/or with CeO_x [33,55], whereas, peak 2 could be associated to Pt NPs interacting with disordered carbon (sp^3) domain [33]. For SMOF-3, the intensity ratio Peak1/Peak2 increases, which could indicate that the peak 1 is related to Pt-CeO_x interaction rather than Pt- sp^2 inter-

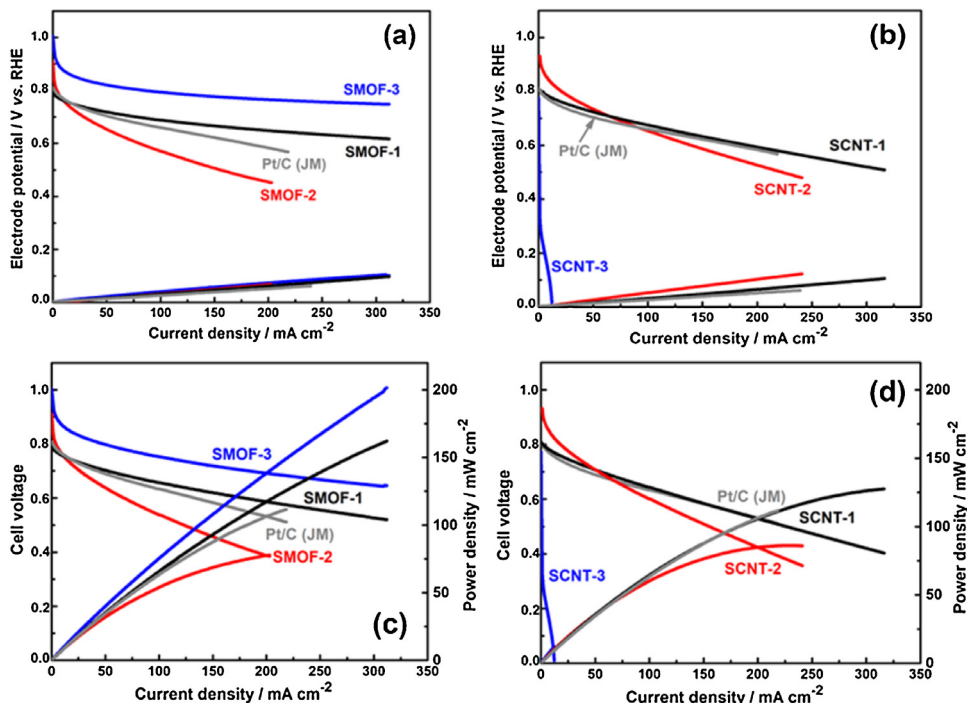


Fig. 8. (a and b) Corresponding representative anode and cathode polarization curves of a H₂/O₂ μ LFFC; and (c and d) cell voltage and power density curves (iR-drop corrected). Pt/C (JM) catalyst was used as anode in all systems. All curves were recorded in 1.0 M HClO₄ at room temperature.

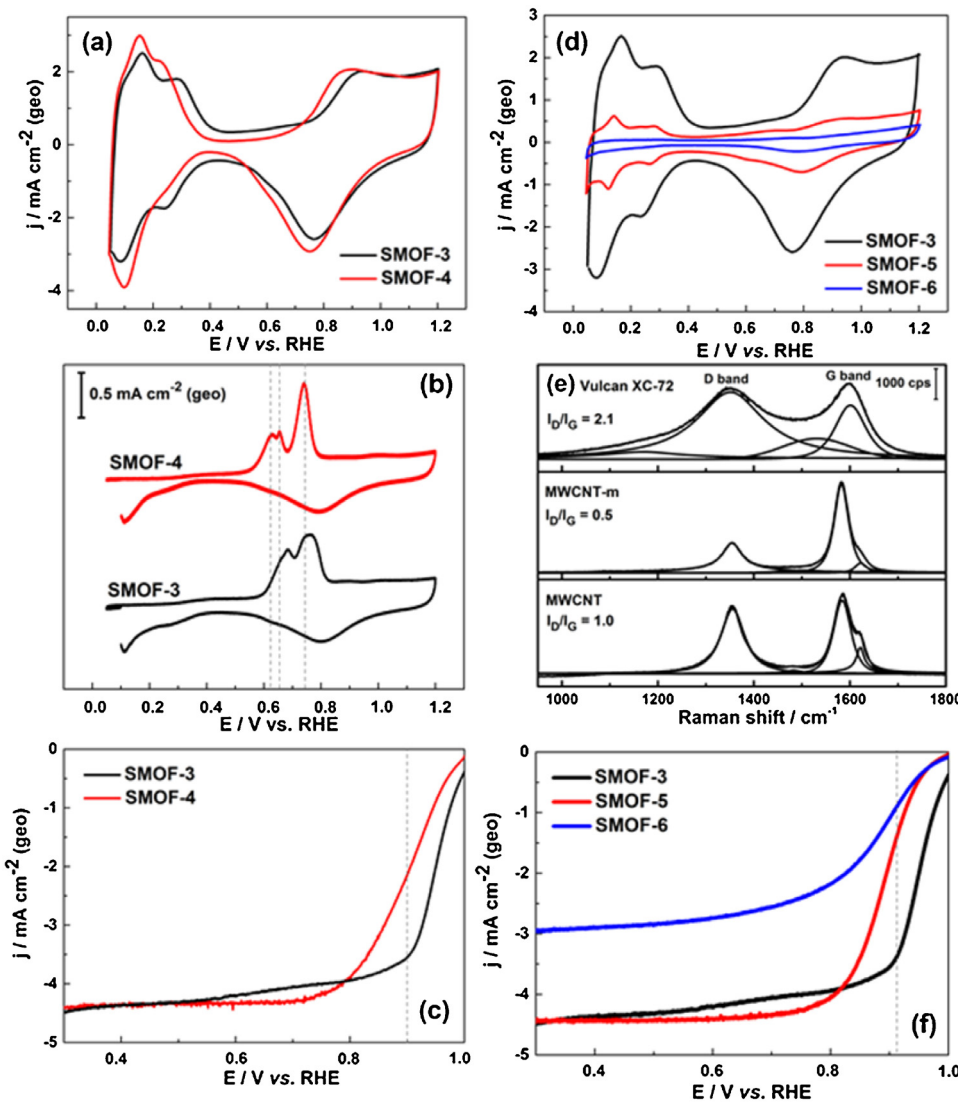


Fig. 9. (a) CVs recorded at scan rate of 50 mV s^{-1} in N_2 -saturated 0.1 M HClO_4 ; (b) CO-stripping voltammograms at scan rate of 5 mV s^{-1} in N_2 -saturated 0.1 M HClO_4 for SMOF-3 and SMOF-4; (c) LSVs on RDE with rotating speed of 900 rpm at scan rate of 5 mV s^{-1} in O_2 -saturated HClO_4 for SMOF-3 and SMOF-4; (d) CVs recorded at scan rate of 50 mV s^{-1} in N_2 -saturated 0.1 M HClO_4 for SMOF-3, SMOF-5 and SMOF-6 samples; (e) Raman spectra for Vulcan XC-72, MWCNT and MWCNT-m materials. (f) LSVs on RDE with rotating speed of 900 rpm at scan rate of 5 mV s^{-1} in O_2 -saturated HClO_4 for SMOF-3, SMOF-5 and SMOF-6 samples.

action. In the literature, the enhancement of Peak1/Peak2 ratio, representing an increased Pt-sp² interaction with respect to Pt-sp³, has been attributed to the decrease of the I_D/I_G (intensity of disordered/graphite domains) ratio obtained via Raman spectroscopy [33]. However, as shown in Fig. 5e, the Raman spectra show I_D/I_G values of ca. 1.1 for SMOF-3, slightly increased with respect to those obtained for MWCNT (ca. 1.0) and SMOF-1 (ca. 1.0). This result would exclude the influence of Pt-sp² interaction on peak 1. Therefore, the Pt-CeO_x interaction should be responsible for the enhancement of the electro-oxidation of CO at lower potentials. For peak 2 in SMOF-3, the peak shape becomes larger, possibly associated to enhanced Pt-sp³ interaction favored within the CeO_x-C composite matrix, because the amount of disordered carbon increased (cf. I_D/I_G ratio in Fig. 5e) due to the decomposition of the MOF precursor. The ECSA values (Table S2) for SMOF samples, deduced from CO-oxidation peak surface, increase upon heating temperature. The ECSA value of SMOF-3 is still higher than the geometric area, suggesting that the adsorption of CO on Pt surface is promoted. For SCNT samples (Fig. 5d), the CO oxidation peak shape and potential is basically the same in SCNT-1 and SCNT-2 samples, though their particle size values are different, excluding the particle

size effect towards CO-stripping for SCNT samples. It can be seen that the potential and shape of peak 1 for SCNT-(1-2) are different from SMOF-3, supporting the Pt/oxide interaction in SMOF-3. For SCNT-3, the I_D/I_G ratio in Raman spectra (Fig. 5e) shows sp³ domain of carbon is dominant rather than sp² domain. Therefore, the phenomenon of missing peak 2 with the negatively shifted peak 1 assesses the CO oxidation is done on larger particles detached from CNT supporting material (as seen from TEM).

3.3. Oxygen reduction reaction on SMOF and SCNT samples in half-cell

The activity of the freshly prepared electrocatalysts towards ORR activity was then investigated; the linear sweep voltammograms (LSV) are reported in Fig. 6. A gradual shift of the half-wave potential ($E_{1/2}$) towards more positive potentials with the heating temperature is observed for SMOF samples (Fig. 6a). This positive shift can be attributed to the formation CeO_x/C composite interacting with the Pt NPs. Conversely, for the SCNT samples (Fig. 6b), a negative shift of $E_{1/2}$ was observed with the heating temperature.

This effect can be associated to the Pt NPs agglomeration with the heat treatment.

In order to further investigate the ORR kinetics, the Tafel slope in the potential interval of 0.96–0.92 V was determined. For the SMOF samples (Fig. 6c), the slope decreases with the heating temperature (from *ca.* –76 mV dec^{–1} for SMOF-1 to *ca.* –52 mV dec^{–1} for SMOF-3), indicating that the Pt/CeO_x/C system has also a positive effect on the ORR kinetics. For the SCNT samples (Fig. 6d), the slope decreases with the heating temperature but the values are higher than the one obtained for the commercial Pt/C (JM) catalyst.

Fig. 6e summarizes the surface specific (SA) and mass activity (MA) for ORR. As seen above, all the SCNT samples and SMOF-1 show a lower activity than the commercial Pt/C (JM) catalyst. However, both SMOF-2 and SMOF-3 have a better performance, with the last one showing higher values than those targeted by the DOE-2015/2017 (Department of Energy, USA) (SA = 770 μA cm^{–2}_{Pt} and MA = 440 mA mg^{–1}_{Pt} at 0.9 V vs RHE in half-cell) [56]. These results further highlight that the presence of CeO_x/C interacting with Pt has an important role in promoting the ORR process. Later on, to study the effect of CeO_x/C, SMOF-3 was subjected to an accelerated durability test (ADT) for the ORR stability in the potential interval of 0.6 V to 1.0 V. The commercial Pt/C (JM) catalyst was used as reference catalyst. The SCNT-2 samples were also subjected to the ADT for comparison to minimize the particle size effect in ORR durability. The evolution of CVs and ORR polarization curves are shown in Fig. S3. The loss of electrochemical active area and activity with the number of cycles is depicted in Fig. 6f. For the commercial Pt/C (JM) and SCNT-2 samples, the active surface area (H_{upd}) and kinetic current density, j_k, decreases with the cycles, and this is reflected in a loss of activity towards ORR. However, the SMOF-3 sample is very stable. TEM images of the SMOF-3 sample after the ADT (Fig. 7a) confirm that there is no agglomeration of the Pt NPs during the cycling treatment and the average particle size does not change. Besides, one can notice that the layer outside the Pt NPs in SMOF-3 becomes thinner after ADT. Conversely, for SCNT-2 catalyst, the TEM (Fig. 7b) shows that morphology and particle size Pt NPs are changed because of the formation of agglomerations after ADT. Considering the results of CO-stripping, these facts reveal that the interaction of Pt-CeO_x, induced by the unique morphology of Pt/CeO_x/C composite should be responsible for ORR stability improvement.

3.4. SMOFs and SCNTs as cathodes in H₂/O₂ micro laminar flow fuel cell (μ LFFC)

The cathodic performance of SMOF and SCNT catalysts were evaluated *via* μ LFFC [57,58]. The commercial Pt/C (JM) catalyst was also tested in the same system for comparison. All data in Fig. 8 are iR-drop corrected (cf. procedure in SI). Fig. 8a shows that a better performance of the μ LFFC system is obtained when the cathode side contains SMOF-3, as expected among other SMOFs, and those labeled SCNTs (Fig. 8b) and commercial Pt/C (JM) catalysts. The performance at the anode side is similar since the commercial Pt/C (JM) catalyst was used in all experiments (cf. Section 4, SI). The cell voltage characteristics as well as the power curves are shown in Fig. 8c and d, and as expected the highest power density is obtained with SMOF-3 in the μ LFFC system. At a current density of *ca.* 200 mA cm^{–2}, the power density on SMOF-3 (*ca.* 129 mW cm^{–2}) is a factor of *ca.* 1.2–1.7 higher than that of SMOF-1, SMOF-2, SCNT-1, SCNT-2 and Pt/C (JM). The cell voltage on SMOF-3 cathode attains 1.0 V. This value is higher than other cathode systems, cf. Fig. 8c and d. Hence, SMOF-3 cathode, in μ LFFC system, outperforms the other cathodes.

3.5. Investigation for the formation of Pt/CeO_x/C composite

The high activity of Pt centers is due to the formation of Pt/CeO_x/C in SMOF-3 catalyst. In order to investigate this issue, the synthesis of Pt NPs deposited on the pre-treated MOF(Ce) mixed with MWCNT, noted as: SMOF-4, was performed. It shows a different surface electrochemical behavior, as contrasted in Fig. 9a and b. The shape of H_{upd} region and the double-layer behavior in CVs, as well as CO-oxidation peak shape and potential, are different from that of SMOF-3. It is worth to be noted that the H_{upd} and CO-oxidation peak surface area for both catalysts are very similar, implying similar amount of Pt active sites. Then again the LSVs (Fig. 9c) illustrates that the ORR activity on SMOF-3 outperforms that of SMOF-4. This should be associated with the special morphology and interaction of CeO_x/C moieties with Pt active sites in SMOF-3 that shows an enhanced ORR activity with respect to SMOF-4. It demonstrates also that the formation of Pt/CeO_x/C composite is an *in-situ* procedure.

Additionally, the carbon, as support, plays an important role in the synthesis of SMOF-3 catalyst. In order to investigate the support effect, besides MWCNT which is used for the synthesis of SMOF-(1–3) and SCNT samples [32], two different carbon were used in the synthesis of Pt/CeO_x/C composites: Vulcan XC-72 [59] (SMOF-5) and MWCNT-m [33] (SMOF-6), *via* the same synthetic procedures. From the Raman spectra on these supports, Fig. 9e, it is clear that the I_D/I_G value follows the trend: XC-72 (*ca.* 2.1) [33] > MWCNT (*ca.* 1.0) > MWCNT-m (*ca.* 0.5) [33]. Then the CVs, depicted in Fig. 9d, show that the SMOF-3 gives much larger H_{upd} surface area than SMOF-5 and SMOF-6 samples. The ORR polarization curves, in Fig. 9f, confirm that the best catalyst is achieved with MWCNT support: the SMOF-3 catalyst. Hence, the formation of highly active Pt/CeO_x/C should also be related to the nature of carbon support.

4. Conclusions

Through this study, we explore the role of a MOF(Ce) as a sacrificial precursor during the synthesis of Pt/CeO_x/C nanocomposite (SMOF-3), and compared to MOF-free samples. From the analysis of pXRD and TEM data, one can conclude that the impact of MOF was unique in forming of CeO_x, intimately contacted to Pt surface, and protecting Pt NPs against agglomeration. The XPS reveals that CeO_x, derived from MOF(Ce), interact with Pt NPs, stabilizing Pt⁰ and Ce³⁺ state in the nanocomposite. The surface electrochemistry of Pt/CeO_x/C nanocomposite is thus modified, showing promoted H and CO adsorption, thus higher Pt active surface area with respect to other SMOF, SCNT and commercial Pt/C (JM) catalyst. The CO-stripping analysis, together with Raman spectra, demonstrates strong interaction between Pt and CeO_x. The ORR activity on SMOF-3 catalyst was observed as highly enhanced with respect to SMOF, SCNT and Pt/C (JM) catalysts, outperforming DOE 2015/2017 target in half-cell. In addition, the ORR stability on SMOF-3, *via* ADT, was improved, in contrast to those oxide-free SCNT-2 and Pt/C (JM) samples. Finally, such an innovative composite was validated as cathode catalyst in a H₂/O₂ μ LFFC system. Compared with other homemade and Pt/C (JM) cathodic catalysts, the cell power density was enhanced by a factor of *ca.* 1.2–1.7. All these facts assess the significant role of CeO_x, based on MOF(Ce) precursor, in the formation of Pt/CeO_x/C nanocomposite, leading to a modified Pt surface and resulting enhanced ORR kinetic and stability. This work has also demonstrated that the novel Pt/CeO_x/C nanocomposite can be *in-situ* prepared at high temperature (900 °C under inert gas) where both MWCNTs and porous carbon are key ingredients. Our study, indeed, extends the application of MOF materials in preparation of Pt-based nanomaterials for energy conversion.

Acknowledgments

This work was supported by the European Union's Seventh Framework Program (FP7/2007–2013) for the Fuel Cell and Hydrogen Joint Technology Initiative under grant agreement nr. 303492–CathCat, and the University of Poitiers, France. All the authors thank Mr. Juan Manuel Mora-Hernandez for some experiments on μ LFFC. The synthesis of Pt/CeO_x/C composite was protected by a patent (**WO2015144894A1**).

Appendix A. Supplementary data

Supplementary data associated with this article can be found, in the online version, at <http://dx.doi.org/10.1016/j.apcatb.2016.02.028>.

References

- [1] W. Yu, M.D. Porosoff, J.G. Chen, *Chem. Rev.* (Washington, DC, U.S.) 112 (2012) 5780–5817.
- [2] Y. Luo, N. Alonso-Vante, *Electrochim. Acta* 179 (2015) 10.
- [3] J. Greeley, I.E.L. Stephens, A.S. Bondarenko, T.P. Johansson, H.A. Hansen, T.F. Jaraillo, J. Rossmeisl, I. Chorkendorff, J.K. Nørskov, *Nat. Chem.* 1 (2009) 552–556.
- [4] S.J. Yoo, K.-S. Lee, S.J. Hwang, Y.-H. Cho, S.-K. Kim, J.W. Yun, Y.-E. Sung, T.-H. Lim, *Int. J. Hydrom. Energy* 37 (2012) 9758–9765.
- [5] M. Escudero-Escribano, A. Verdaguera-Casadevall, P. Malacrida, U. Grønbjerg, B.P. Knudsen, A.K. Jepsen, J. Rossmeisl, I.E.L. Stephens, I. Chorkendorff, *J. Am. Chem. Soc.* 134 (2012) 16476–16479.
- [6] M.K. Jeon, P.J. McGinn, *J. Power Sour.* 196 (2011) 1127–1131.
- [7] Y. Luo, A. Habrioux, L. Calvillo, G. Granozzi, N. Alonso-Vante, *ChemPhysChem* 15 (2014) 2136–2144.
- [8] K.G. Nishanth, P. Sridhar, S. Pitchumani, *Electrochim. Commun.* 13 (2011) 1465–1468.
- [9] P. Hernandez-Fernandez, F. Masini, D.N. McCarthy, C.E. Strel, D. Friebel, D. Deiana, P. Malacrida, A. Nierhoff, A. Bodin, A.M. Wise, J.H. Nielsen, T.W. Hansen, A. Nilsson, E.L. Stephens, I. Chorkendorff, *Nat. Chem.* 6 (2014) 732–738.
- [10] Y. Luo, A. Habrioux, L. Calvillo, G. Granozzi, N. Alonso-Vante, *ChemCatChem* 7 (2015) 1573–1582.
- [11] P. Bera, A. Gayen, M.S. Hegde, N.P. Lalla, L. Spadaro, F. Frusteri, F. Arena, *J. Phys. Chem. B* 107 (2003) 6122–6130.
- [12] N. Alonso-Vante, *Fuel Cells* 6 (2006) 182–189.
- [13] L. Yang, S. Kinoshita, T. Yamada, S. Kanda, H. Kitagawa, M. Tokunaga, T. Ishimoto, T. Ogura, R. Nagumo, A. Miyamoto, M. Koyama, *Angew. Chem.* 122 (2010) 5476–5479.
- [14] J.-R. Li, R.J. Kuppler, H.-C. Zhou, *Chem. Soc. Rev.* 38 (2009) 1477–1504.
- [15] Y. Qiu, H. Deng, S. Yang, J. Mou, C. Daiguebonne, N. Kerbellec, O. Guillou, S.R. Batten, *Inorg. Chem.* 48 (2009) 3976–3981.
- [16] S. Freslon, Y. Luo, G. Calvez, C. Daiguebonne, O. Guillou, K. Bernot, V. Michel, X. Fan, *Inorg. Chem.* 53 (2014) 1217–1228.
- [17] X. Yi, K. Bernot, F. Pointillart, G. Poneti, G. Calvez, C. Daiguebonne, O. Guillou, R. Sessoli, *Chem. Eur. J.* 18 (2012) 11379–11387.
- [18] J. Lee, O.K. Farha, J. Roberts, K.A. Scheidt, S.T. Nguyen, J.T. Hupp, *Chem. Soc. Rev.* 38 (2009) 1450–1459.
- [19] Y. Fu, D. Sun, Y. Chen, R. Huang, Z. Ding, X. Fu, Z. Li, *Angew. Chem.* 124 (2012) 3420–3423.
- [20] C. Wang, Z. Xie, K.E. deKrafft, W. Lin, *J. Am. Chem. Soc.* 133 (2011) 13445–13454.
- [21] H.-L. Jiang, Q. Xu, *Chem. Commun. (Cambridge, U. K.)* 47 (2011) 3351–3370.
- [22] A.K. Singh, Q. Xu, *ChemCatChem* 5 (2013) 3000–3004.
- [23] C. Wang, K.E. deKrafft, W. Lin, *J. Am. Chem. Soc.* 134 (2012) 7211–7214.
- [24] C.O. Ania, M. Seredych, E. Rodriguez-Castellon, T.J. Bandosz, *Appl. Catal. B* 163 (2015) 424–435.
- [25] J. Shui, C. Chen, L. Grabstanowicz, D. Zhao, D.-J. Liu, *Proc. Natl. Acad. Sci. U. S. A.* 112 (2015) 10629–10634.
- [26] T.B. Čelič, M. Grilc, B. Likozar, N.N. Tušar, *ChemSusChem* 8 (2015) 1703–1710.
- [27] Q. Li, P. Xu, W. Gao, S. Ma, G. Zhang, R. Cao, J. Cho, H.-L. Wang, G. Wu, *Adv. Mater. (Weinheim, Ger.)* 26 (2014) 1378–1386.
- [28] J.-W. Jeon, R. Sharma, P. Meduri, B.W. Arey, H.T. Schaef, J.L. Lutkenhaus, J.P. Lemmon, P.K. Thallapally, M.I. Nandasiri, B.P. McGrail, S.K. Nune, *ACS Appl. Mater. Interfaces* 6 (2014) 7214–7222.
- [29] M. Jahan, Q. Bao, K.P. Loh, *J. Am. Chem. Soc.* 134 (2012) 6707–6713.
- [30] Y. Luo, G. Calvez, S. Freslon, C. Daiguebonne, T. Roisnel, O. Guillou, *Inorg. Chim. Acta* 368 (2011) 170–178.
- [31] T. Masuda, H. Fukumitsu, K. Fugane, H. Togasaki, D. Matsumura, K. Tamura, Y. Nishihata, H. Yoshikawa, K. Kobayashi, T. Mori, K. Uosaki, *J. Phys. Chem. C* 116 (2012) 10098–10102.
- [32] A. Orfanidi, M.K. Daleton, S.G. Neophytides, *Appl. Catal. B* 106 (2011) 379–389.
- [33] J. Ma, A. Habrioux, C. Morais, A. Lewera, W. Vogel, Y. Verde-Gómez, G. Ramos-Sánchez, P.B. Balbuena, N. Alonso-Vante, *ACS Catal.* 3 (2013) 1940–1950.
- [34] Y. Luo, J.M. Mora-Hernández, L.A. Estudillo-Wong, E.M. Arce-Estrada, N. Alonso-Vante, *Electrochim. Acta* 173 (2015) 771–778.
- [35] R.E. Dinnebier, S.J.L. Billinge (Eds.), (RSC publishing (2008)).
- [36] M. Wojdyr, *J. Appl. Crystallogr.* 43 (2010) 3.
- [37] A.J. Bard, L.R. Faulkner, *Electrochemical Methods: Fundamentals and Applications*, Second ed., John Wiley&Sons, New York, 2001.
- [38] L. Wang, P. Yu, L. Zhao, C. Tian, D. Zhao, W. Zhou, J. Yin, R. Wang, H. Fu, *Sci. Rep.* 4 (2014).
- [39] Y. Luo, PhD Thesis, Université de Rennes 1, 2012.
- [40] W. Vogel, L. Timperman, N. Alonso-Vante, *Appl. Catal. A* 377 (2010) 167–173.
- [41] J.-H. Kim, S. Chang, Y.-T. Kim, *Appl. Catal. B* 158–159 (2014) 112–118.
- [42] J.I. Langford, D. Louer, P. Scardi, *J. Appl. Crystallogr.* 33 (2000) 964–974.
- [43] D. Chataigne, *Combined Analysis*, John Wiley & Sons, 2010.
- [44] E. Said-Galiyev, A. Nikolaev, E. Levin, E. Lavrentyeva, M. Gallyamov, S. Polyakov, G. Tsirlina, O. Petrii, A. Khokhlov, *J. Solid State Electrochem.* 15 (2011) 623–633.
- [45] A. Weibel, R. Bouchet, F. Boule, P. Knauth, *Chem. Mater.* 17 (2005) 2378–2385.
- [46] Y. Takasu, N. Ohashi, X.G. Zhang, Y. Murakami, H. Minagawa, S. Sato, K. Yahikozawa, *Electrochim. Acta* 41 (1996) 2595–2600.
- [47] Y. Takasu, T. Iwazaki, W. Sugimoto, Y. Murakami, *Electrochim. Commun.* 2 (2000) 671–674.
- [48] L. Artiglia, S. Agnoli, M.C. Paganini, M. Cattelan, G. Granozzi, *ACS Appl. Mater. Interfaces* 6 (2014) 20130–20136.
- [49] U. Berner, K.-D. Schierbaum, *Phys. Rev. B* 65 (2002) 235404.
- [50] M. Nesselberger, S. Ashton, J.C. Meier, I. Katsounaros, K.J.J. Mayrhofer, M. Arenz, *J. Am. Chem. Soc.* 133 (2011) 17428–17433.
- [51] F. Maillard, M. Eikerling, O.V. Cherstouk, S. Schreier, E. Savinova, U. Stimming, *Faraday Discuss.* 125 (2004) 357–377.
- [52] J. Solla-Gullón, F.J. Vidal-Iglesias, E. Herrero, J.M. Feliu, A. Aldaz, *Electrochim. Commun.* 8 (2006) 189–194.
- [53] P. Urchaga, S. Baranton, C. Coutanceau, G. Jerkiewicz, *Langmuir* 28 (2011) 3658–3663.
- [54] F. Maillard, S. Schreier, M. Hanzlik, E.R. Savinova, S. Weinkauf, U. Stimming, *Phys. Chem. Chem. Phys.* 7 (2005) 385–393.
- [55] J. Ma, E. Valenzuela, A.S. Gago, J. Rousseau, A. Habrioux, N. Alonso-Vante, *J. Phys. Chem. C* 118 (2014) 1111–1117.
- [56] M.K. Debe, *Nature* 486 (2012) 43–51.
- [57] A.S. Gago, Y. Gochi-Ponce, Y.-J. Feng, J.P. Esquivel, N. Sabaté, J. Santander, N. Alonso-Vante, *ChemSusChem* 5 (2012) 1488–1494.
- [58] L. Timperman, A.S. Gago, N. Alonso-Vante, *J. Power Sour.* 196 (2011) 4290–4297.
- [59] H. Yang, N. Alonso-Vante, J.-M. Léger, C. Lamy, *J. Phys. Chem. B* 108 (2004) 1938–1947.